metals

MDPI

Article

Understanding the Interdependence of Penetration Depth and Deformation on Nanoindentation of Nanoporous Silver

Yannick Champion [1,*], Mathilde Laurent-Brocq [2], Pierre Lhuissier [1], Frédéric Charlot [3], Alberto Moreira Jorge Junior [1,4,5] and Daria Barsuk [1]

[1] Univ. Grenoble Alpes, CNRS, *SIMaP*, 38000 Grenoble, France; pierre.lhuissier@simap.grenoble-inp.fr (P.L.); moreira@ufscar.br (A.M.J.J.); dashaadak91@gmail.com (D.B.)
[2] Institut de Chimie et des Matériaux Paris-Est, CNRS-UPEC, 2 rue Henri Dunant 94320 Thiais, CEDEX, France; laurent-brocq@icmpe.cnrs.fr
[3] Univ. Grenoble Alpes, *CMTC*, 38000 Grenoble, France; frederic.charlot@grenoble-inp.fr
[4] Univ. Grenoble Alpes, CNRS, *LEPMI*, 38000 Grenoble, France
[5] Federal University of São Carlos, DEMa, São Paulo 13565-905, Brazil
* Correspondence: yannick.champion@simap.grenoble-inp.fr; Tel.: +33-476-826-749

Received: 31 October 2019; Accepted: 11 December 2019; Published: 14 December 2019

Abstract: A silver-based nanoporous material was produced by dealloying (selective chemical etching) of an $Ag_{38.75}Cu_{38.75}Si_{22.5}$ crystalline alloy. Composed of connected ligaments, this material was imaged using a scanning electron microscope (SEM) and focused ion-beam (FIB) scanning electron microscope tomography. Its mechanical behavior was evaluated using nanoindentation and found to be heterogeneous, with density variation over a length scale of a few tens of nanometers, similar to the indent size. This technique proved relevant to the investigation of a material's mechanical strength, as well as to how its behavior related to the material's microstructure. The hardness is recorded as a function of the indent depth and a phenomenological description based on strain gradient and densification kinetic was proposed to describe the resultant depth dependence.

Keywords: nanoporous metallic alloy; nanoindentation; hardness; strain gradient

---

1. Introduction

Metallic nanoporous (NP) materials present interesting perspectives owing to their nanometric-size microstructure and large specific surface (extremely high open-porosity level). From the first feature, mechanical strength, unique plasticity, and multiphysical properties are expected [1–5]. The second is related to surface interactions and chemical reactivity, with perspectives in domains such as electrochemical energy storage and conversion, catalysts [6,7], biomedical implants [8], and filtering and purification [9]. Based on its design and fabrication, this novel material family has been the subject of intensive fundamental research [10–12], as well as characterization at various levels of microstructure, topology, and morphology [13–16].

In this article, we report on the mechanical behavior of silver nanoporous materials via the analysis of instrumented nanoindentation measurements. Materials were produced by dealloying (selective chemical etching) of the $Ag_{38.75}Cu_{38.75}Si_{22.5}$ crystalline alloy, initially studied for its electrocatalytic properties [17]. Usually, indentation testing provides a preliminary insight into the mechanical properties of materials (strength, ductile/fragile character, toughness) [18,19]. For crystalline solids, the strength σ_s is simply derived from the Tabor rule for metallic alloys: $H \approx 3\sigma_s$ where H is the Vickers hardness.

The specific feature of indentation investigated in this paper was the dependence between the hardness measured and the indent size [20]. Such dependence can be explained using the Ashby rule: a non-symmetric plastic deformation (as in an indentation where deformation is confined) generates a strain gradient in the deformation zone. For crystalline solids, the strain gradient leads to extra hardening, which Ashby described in terms of geometrically necessary dislocations (GND) [21]. Using this approach, Nix and Gao showed that the depth-dependence hardness for crystalline and ductile solids follows the rule: $H/H_0 = \sqrt{1+h^*/h}$ where h^* is a material constant and H_0 the hardness at a hypothetical infinite indent size [22].

For non-crystalline solids, the rule is obviously different since dislocations are nonexistent. In metallic glasses, deformation is localized in thin shear bands leading to the absence of macroscopic plasticity when they are tested using tension or compression. However, plasticity can be observed in the indentation owing to the confined character of the testing. Similarly with crystalline solids, a depth dependence of the hardness was observed but with a slightly different rule: $H/H_0 = 1 + \sqrt{h^*/h}$ [23].

Whatever the material and defects involved in the plastic deformation, it was observed that the Ashby rule on strain gradient is generalized. As far as a strain gradient is defined, size dependence can be analytically expressed as this was demonstrated for metallic glasses [24]. Here we report on depth dependence in the nanohardness testing of nanoporous silver, with the rule that follows: $H/H_0 = 1 + h^*/h$. A phenomenological description of the nanohardness variation with regard to indent size was proposed, fitting the experimental observations. The modeling was based on the strain gradient induced by local densification, which was related to ligament rearrangement. This analysis provided a proper evaluation of the mechanical strength of nanoporous metal, as well as giving an insight into material dynamical evolution during deformation.

2. Experiments

2.1. Formation of Nanoporous Materials

Ag-based polycrystalline alloy with the composition $Ag_{38.75}Cu_{38.75}Si_{22.5}$ was prepared by arc melting pure Ag, Cu, and Si (99.99% purity, Alfa Aesar, Kandel Germany) in a helium atmosphere. Five successive melting steps were employed to ensure alloy homogeneity, and then rapid solidification casting of the alloy was performed on a rotating copper wheel. Foils with thicknesses ranging from 20 to 60 µm were produced by varying the rotating speed of the copper wheel. As reported in [17], the cast ribbon analyzed by X-ray diffraction was constituted by fcc Ag(Si) solid solution and hexagonal Cu_3Si. Dealloying of the as-cast ribbons was performed at ambient temperature using two chemical etchants [25]: 13.4 wt% 2.12 M of HNO3, and 0.67 M of HNO3 and 0.64 M of HF in deionized water. The second etchant was used to accelerate the dissolution of Si atoms, resulting in a more regular microstructure and composition of the matrix, minimizing the content of residual Si and Cu elements. Full details of the materials' synthesis and characterization are reported in [17].

The materials were characterized using SEM (Zeiss Ultra 55, Oberkochen, Germany) complemented by tomographic imaging, using focused ion-beam slice cutting and image reconstruction (Carl ZEISS Cross Beam NVision FIB, Ga ion with an acceleration voltage of 30 kV and current intensity of 300 pA). After each etching, imaging of the freshly exposed material cross-section was recorded using the SEM. The stack of images was processed to generate the dissected volume of interest, producing a three-dimensional representation of the alloy's microstructure. To capture the nanostructure with an average length scale of about 50 nm, slices of 5 nm were cut (voxel of $5 \times 5 \times 5$ nm^3) and the thickness analyzed was of the order of 250 nm.

Reconstruction of the 3D images were performed using ImageJ/Fiji (NIH, Bethesda, MD, USA) and Avizo software (Thermo Scientific, Waltham, MA, USA) as well as a homemade plugin [26]. Nanoindentations were performed using a HysitronTI950 (Bruker, Eden Prairie, MN, USA) with a Berkovitch diamond tip. The surface topography and indents were imaged using the scanning-probe microscopy mode of the nanoindenter, which consisted of scanning the sample surface with the nanoindenter tip. Focused ion-beam (FIB) cutting of an indented zone of the material was also performed for detailed analysis and modeling.

First, quasistatic measurements, with a maximum load of 900 and 10,000 µN, a loading rate of 100 µN/s, and a holding time of 2 s, were performed. Second, dynamic mechanical analysis (DMA), which is also known as the continuous stiffness measurement (CSM), was used to continuously measure hardness and the Young modulus as a function of depth. A constant strain-rate loading of 0.15 s^{-1} was applied—up to a maximum load of 10,000 µN—and was maintained for 2 s, after which unloading at a constant rate was then performed. The oscillating frequency was set to 220 Hz.

In this study, two nanoporous materials NP1 and NP2 were compared. They were dealloyed for 45 and 180 min, respectively, and showed different structures in terms of density, ligament size, and connectivity. The average size and diameter of ligaments was estimated from a series of measurements using the Straight Line function of ImageJ and statistical analyses. The apparent porosity level was estimated from the surface of the SEM image after thresholding and evaluation of a fraction of the white pixels present. With these materials, multiple nanoindentation experiments at various positions on the samples' surface were carried out and averaged. Finally, the hardness and Young's modulus were determined using the Oliver–Pharr method [27].

2.2. Nanoporous Structure

Comparison between nanoporous metals NP1 and NP2 (Figure 1) was made in an attempt to reveal structural characteristics involved in nanoindentation size effect. This approach was consistent, as the materials showed different sizes in their microstructure but similar microstructural characteristics (morphology and topology). From a nanoporous formation, where coarsening is controlled by the surface diffusion, self-similarity (scale independent microstructure) is usually expected, although the existence of phenomenon is still subject to debate. Here the self-similarity is the ability of the material to coarsen during dealloying while maintaining its structural characteristics. This is seldom observed, however, because the time scale of the experiments usually places them in a transient domain of the process [16].

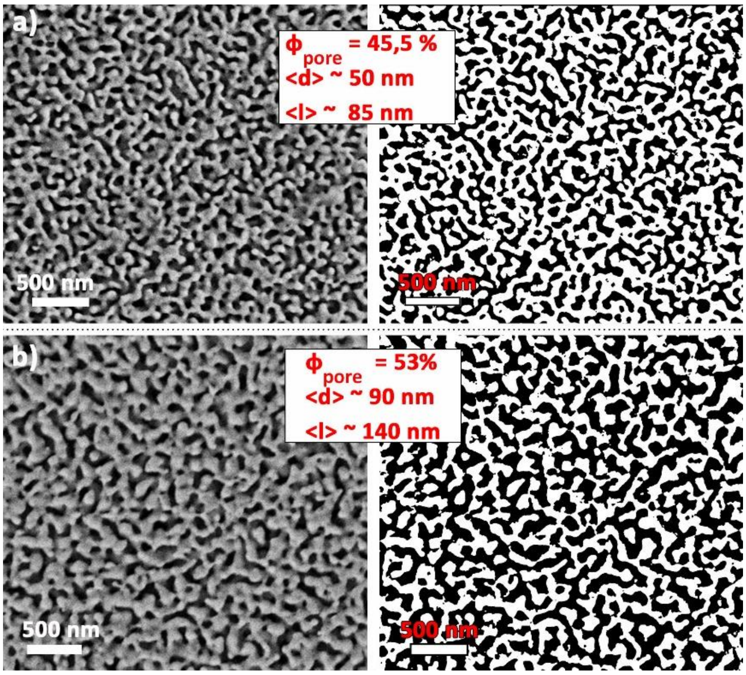

Figure 1. SEM (scanning electron microscope) secondary electron images of a nanoporous (NP) material and corresponding threshold patterns as a binary generated image: (**a**) NP1, dealloying time of 45 min and (**b**) NP2, dealloying time of 3 h.

A FIB tomographic image of a nanoporous silver similar to NP1 and NP2 showed the microstructural complexity in terms of morphological and topological characteristics. This type of analysis provided us with the local surface shape (Figure 2a) and curvedness level (Figure 2b), and from them a surface shape–curvedness statistical distribution (Figure 2c). This was a useful structural function of the material for properties analysis (shape index and curvedness are calculated from the principal curvatures κ_1 and κ_2)

$$S = \frac{2}{\pi}\arctan\frac{\kappa_1 + \kappa_2}{\kappa_1 - \kappa_2} \text{ and } C = \sqrt{\frac{\kappa_1^2 + \kappa_2^2}{2}}$$

These parameters were of particular interest in the understanding and modeling of an NP material's properties. For example, its curvature ended up affecting its mechanical properties through the Laplace law and chemical properties through the Gibbs-Thomson law, with a dominant effect at the nanoscale level. This complexity makes it rather difficult to prove a real similarity between different specimens.

However, to help in our work, simple visual comparison was made between NP1 and a rescaled NP2, though differences in porosity did not allow for full adaptation. The scaling factor used was the ratio between different porosities, and the superimposition in Figure 3 makes a convincing case for near-similarity, at least on the 2D SEM images.

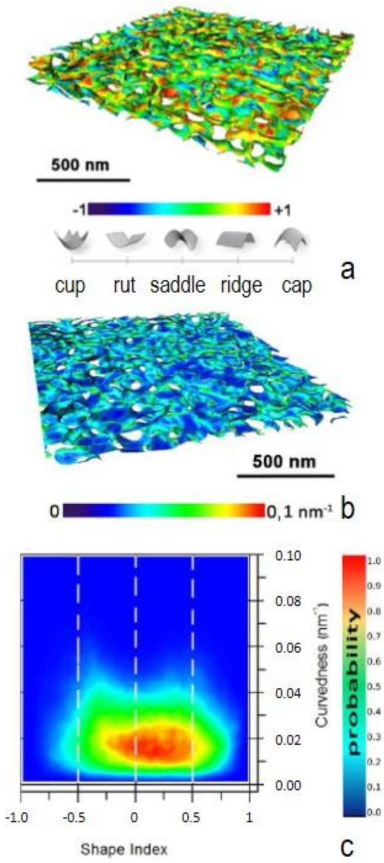

Figure 2. Tomographic perspective views of the nanoporous silver via focused ion-beam (FIB) scanning electron microscope slice cutting and computer image reconstruction. Color mapping surface according to its classification of shape index (**a**); and curvedness (**b**); (**c**) 2D view of the surface shape and curvedness distributions.

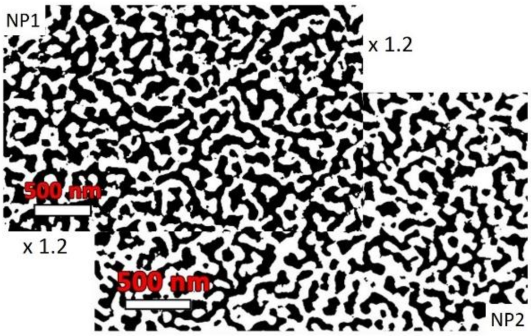

Figure 3. Visual evaluation of self-similarity between NP1 and NP2 by superimposition after rescaling NP1 by a factor of 1.2.

2.3. Nanoindentation

With a probe (indentation tip) size in the order of the length scale of the cellular microstructure, interpretations and quantitative analyses from the nanoindentation of nanoporous materials were challenging and subject to debate. Preliminary studies were undertaken to evaluate these length–scale issues. A series of more than 50 nanoindentations in quasistatic condition were performed on NP1 and NP2. A selection of 4 different indentations taken from the NP2 series and compared with a bulk silver sample were as seen in Figure 4. Every loading curve (see the inset of Figure 4) exhibited 2 successive extended bumpy regions (diffuse serrations).

The first region had a penetration depth of ~30 nm, which was probably not relevant and likely due to the Berkovitch tip edge imperfections (roughness, irregularities). The second one extended from about 50 to 150 nm, which was of the order of the NP microstructure length scale and over which the tip was alternately probing pores and ligaments. Despite fluctuations in the loading curves, it is interesting to observe from Figure 5, that an indent was already clearly formed at an approximate depth of 70 nm in the bumpy region, and likely useable throughout our statistical series analyses.

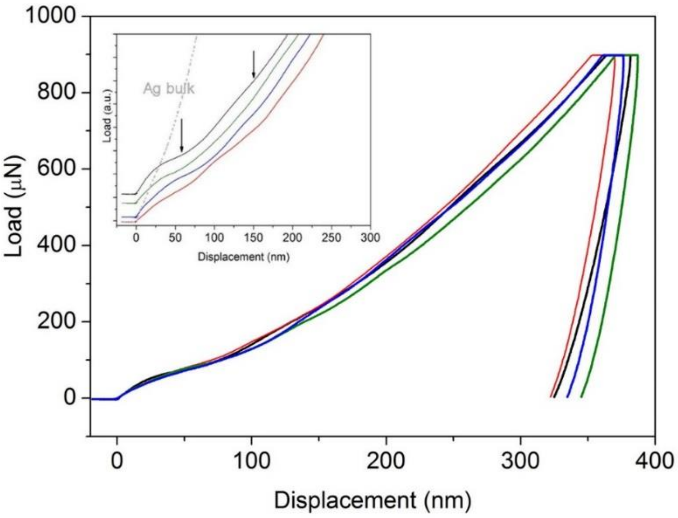

Figure 4. Selection of indentation curves on various positions of the sample of NP2. The inset shows the details of the diffuse serrations at an early stage of deformation and its comparison with bulk silver.

As usual, an apparent (size-effect affected) hardness was drawn from the maximum load $F_{\max}$ and depth h using $H = F_{\max}/24.5 \times h^2$, averaged over the indentation series for NP1 and NP2, respectively, and thus giving H_{NP1} = 250 ± 2 MPa and H_{NP2} = 240 ± 10 MPa. From the unloading part of the curves, $E_r = \frac{dF}{dh} \times \frac{1}{C\sqrt{A_{\max}}}$, which was a good estimation of the elastic modulus of the material. The modulus values were E_{NP1} = 20.7 ± 3.2 GPa and E_{NP2} = 12.7 ± 5.5 GPa for NP1 and NP2, respectively.

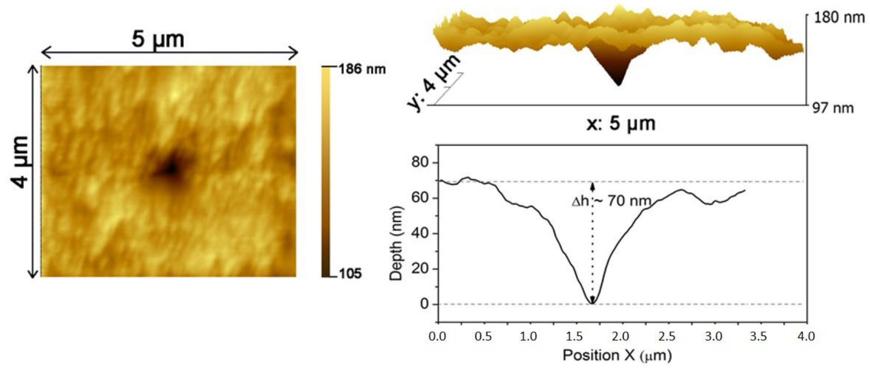

Figure 5. Scanning probe microscopy of the surface, and profile image of the slow-rate quasistatic indent, which reached a final depth of 70 nm after elastic relaxation.

The depth dependence was investigated using the DMA mode of the indenter, allowing us to keep an ongoing measurement of the hardness as a function of depth. In Figure 6a,b, the overall plot of H as a function of $1/h$ showed a maximum value at about 30 nm, which was of the order of the lower limit for a relevant measure due to tip imperfections (Figure 6a,b). H as a function of $1/h$ was suggested as the best linear plot for the test series seen in Figure 6c,d. For h larger than 40–50 nm, which corresponded to the upper part of the bumpy region, the data are plotted Figure 6c,d for NP1 and NP2, respectively. From the linear fit, hardness at a hypothetical infinite indent size ($h \to \infty$) when none were affected by size effect was obtained respectively for NP1 and NP2, H_{01} = 58 ± 10 MPa and H_{02} = 163 ± 18 MPa. The slope (α) related to the size-effect sensitivity informed other deformation dynamics of the NP metal: α_1 = 67 ± 8 GPa·nm and α_2 = 47 ± 15 GPa·nm for NP1 and NP2, respectively.

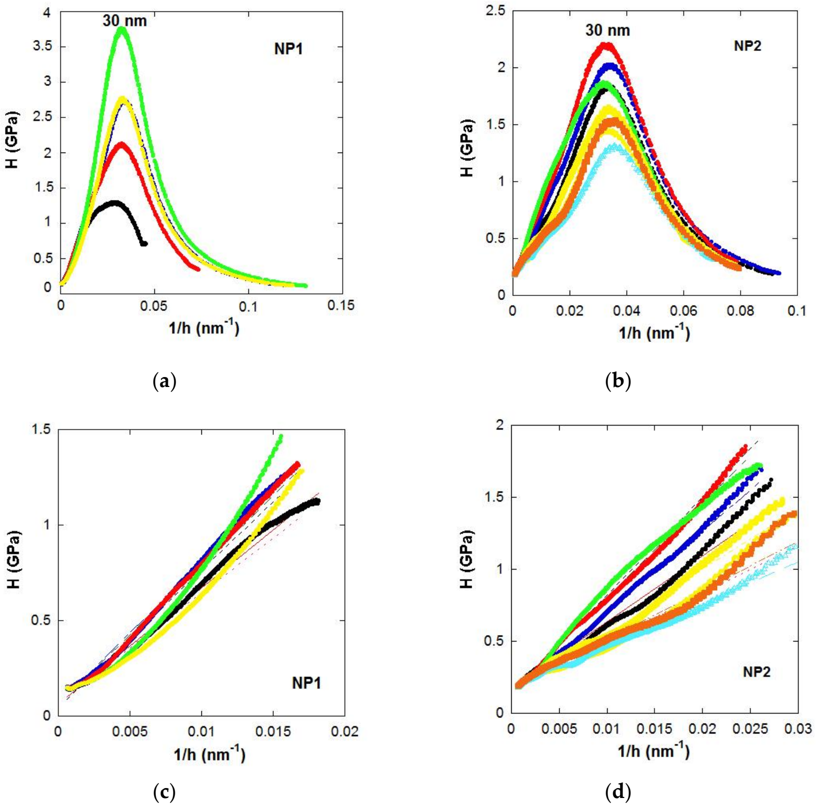

(**a**) (**b**)

(**c**) (**d**)

Figure 6. Plots of series of hardness as a function of 1/h from dynamic mechanical analysis (DMA) analyses for NP1 (**a**,**c**) and NP2. (**b**,**d**). (**c**,**d**) are zoomed in at a low 1/h of (**a**,**b**). Linear fittings of the curves were plotted as straight or dashed lines on (**c**,**d**).

3. Depth Dependence of Hardness

An analytical description of the size effect in a phenomenological approach was proposed to interpret the hardness value in the experimental data. The hardness H was the ratio of the applied load F to the area $A(h)$ produced by the penetration of the indent in the materials. F was arbitrarily fixed and the resulting area $A(h)$ was such that H became a function of h. This could be written as the sum of a constant hardness and an additional variable hardness dependent on h:

$$\begin{gathered} H = \frac{F}{A(h)} = \frac{F_0(h)}{A(h)} + \frac{f(h)}{A(h)} \\ \text{with, and } \forall h,\ \frac{F_0(h)}{A(h)} = H_0, H \to H_0 \ \text{ or } \frac{f(h)}{A(h)} \to 0 \ \text{ for } h \to \infty \end{gathered} \tag{1}$$

The projected area was $A(h) = Ah^2$ with $A = 24.56$ for Berkovitch indent geometry (Figure 7). Then, the local force on an infinitesimal surface $dA(h)$ at height h was derived as:

$$df(h) = \sigma(h) \times 2Adh \tag{2}$$

where $\sigma(h)$ was the local back stress induced by the confinement of the deformation. The Ashby rule regarding strain gradient [21] predicted the stress $\sigma(h)$ at height h, following: $(\sigma(h)/\sigma_0)^2 = l\gamma/h$, where σ_0 and l were the stress and length scale parameters, respectively.

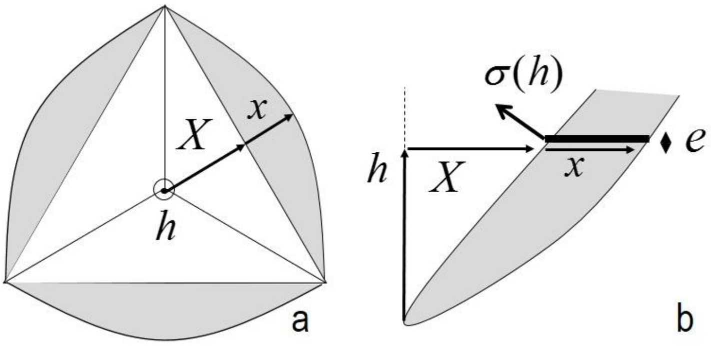

Figure 7. Scheme of a Berkovitch indent with the strained zone denoted in grey. (**a**) Top view, (**b**) cross-section view of a third of the indent. The parameters used in this modeling are as shown: indent shear X applied at height h, and the resulting shear displacement x of an NP infinitesimal thickness e. $\sigma(h)$ was the resulting back stress produced at height h from the strain gradient.

For highly porous materials made of plastic ligaments, densification was the main deformation mechanism when compressed. In this way, the strain gradient could be readily attributed to the variation in densification along the indent surface. This assumption was verified qualitatively by cutting an indent using the FIB technique and analyzing ligament distributions at various heights. This was imaged by plotting the greyscale distribution, along with a line scan for two different zones of the indent (Figure 8). We observed that the frequency of the greyscale variation was larger at more profound locations than when compared to the zone just below the sample surface.

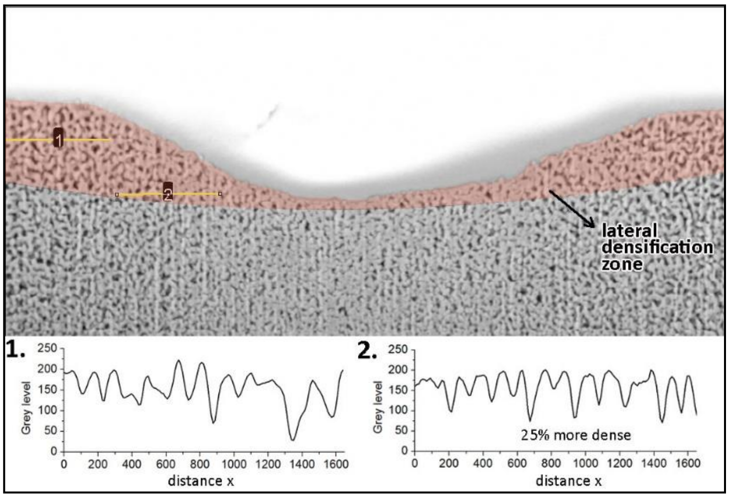

Figure 8. SEM image displaying the FIB (focused ion-beam) cross-section of an indent made on an NP1, up to 1.4 µm in depth. The insets show grey-level variation along lines 1 and 2 that correspond to the less and more densified regions of the deformed volume under the indent.

Our modeling consisted of defining the pertinent expression for the Ashby strain gradient to the insert in Equation (1) of the hardness. At the height h, strain was defined as $\gamma = 1 - \frac{x}{X}$ (as seen in Figure 7a,b). X was the displacement produced by the indent, and x the resulting displacement in the material. The difference between X and x was due to densification which varied as a function of h as shown on Figure 8. In a thin slice e at height h, densification was evaluated via volume variation. Considering the relative density $D = \rho/\rho_0$, with ρ and ρ_0 representing, respectively, the volume weight of the nanoporous and bulk materials, it can be shown that (The width of the impacted zone was proportional to h, with p a proportionality factor depending on the indent shape, v the volume of the densified region (Figure 7), and with $v = phex$, at h, the volume variation in the thin slice e was $dv = phedx$. Dividing by the weight of the slice and introducing the volume weight ρ it becomes, and eventually $\frac{dD}{D} = d\gamma$)

$$\frac{dD}{D} = d\gamma \tag{3}$$

The densification, which was a positive variation of D in the porous media, could be attained by the densification dynamics of powders proposed by Shapiro and Kolthoff et al. [28]. It has been conjectured that the porosity $(1 - D)$ variation as a function of the applied pressure follows a 1st-order kinetics law, which at a constant stress rate can be written:

$$-\frac{d(1-D)}{d\sigma} = k(1-D) \tag{4}$$

and with (3): $\frac{d\gamma}{d\sigma} = k(\frac{1}{D} - 1)$.

Deriving the Ashby rule, $2\sigma(h)d\sigma(h)/{\sigma_0}^2 = ld\gamma/h$ gave us an equation for the back stress generated by the densification gradient: $\sigma(h) = \frac{{\sigma_0}^2 l}{2h} \times \frac{d\gamma}{d\sigma(h)}$. Combined with Equation (4) gave us:

$$\sigma(h) = \frac{{\sigma_0}^2 lk}{2} \times (\frac{1}{D} - 1) \times \frac{1}{h} \tag{5}$$

It was easily shown (see [24]) that $\frac{f(h)}{A(h)} = \sigma(h)$, and with Equation (1) the hardness dependence in relation to the indent depth was eventually derived:

$$H = H_0 + \frac{{\sigma_0}^2 lk}{2} \times (\frac{1}{D} - 1) \times \frac{1}{h} \tag{6}$$

As observed experimentally, this relation shows the dependance the material hardness on the inverse of the depth considered.

4. Discussion

The mechanical properties of foam, cellular, or porous materials as a function of their porosity were systematically examined with respect to the Gibson–Ashby scaling law on hardness and elastic modulus [29]. In our analyses, the hardness of NP1 and NP2 could not be evaluated because the hardness of the material (Ag) forming ligament was unknown. In contrast to this, elastic modulus was could be well evaluated from quasistatic nanoindentation experiments.

From the Gibson–Ashby law $E_{NP} = E \times D^2$ and with an elastic modulus of bulk Ag measured under the same conditions $E \approx 76 \pm 2.5$ GPa, the moduli of NP1 and NP2 were calculated respectively as $E_{NP1}^{calc} \approx 22.6$ GPa and $E_{NP2}^{calc} \approx 16.8$ GPa, and compared to measured values $E_{NP1} = 20.7 \pm 3.2$ GPa and $E_{NP2} = 12.7 \pm 5.5$ GPa.

Our work mainly focused on the size dependence of hardness in nanoindentation of NP metals where their analytical description brought some interesting insights into NP deformation as controlled by densification. The parameters in Equation (6) describing H as a function of $1/h$ are hereafter discussed. First and most satisfactorily of all, was our finding that parameter $(\frac{1}{D} - 1)$ implied that the material was porous and had densification ability. A drastic limitation on this finding, however, was that to uphold linear dependence this parameter must be also nearly constant, which meant that the variation of the relative density produced during deformation was negligible before D.

From the Ashby rule on strain gradient, σ_0 was the stress scaling parameter and was related to the elastic properties of the ligament material. l was a scaling length parameter and comes from the rule that for a given strain gradient, the back stress is as large as l is large. This indicated that l was related to the densification ability of the NP material. Similarly, the parameter k from the Shapiro–Kolthoff relation also characterizes the ability of the porous material to increase in density under a given incremental stress. We showed that k correlated to the yield strength of the ligament material in its bulk form, following $k \propto 1/\sigma_y$ where σ_y was the yield strength [30] (Note: In the original work, this was the powder particle's material strength in its bulk form).

Comparing NP1 and NP2, the measured slopes ($\alpha_1 = 67 \pm 8$ GPa·nm and $\alpha_2 = 47 \pm 15$ GPa·nm.) show that NP1 had a larger propensity for densification than NP2. This was in contrast to the respective porosity levels of the NPs. The porosity of NP2 was greater, ($(\frac{1}{D} - 1) = 0.83$ and 1.13 for NP1 and NP2, respectively) and the resultant larger space should therefore allow for a greater degree of densification. Assuming σ_0 was nearly the same for both NPs, the dominant effect was related to the NPs ability for densification (characterized by $k \times l$) which was shown as larger for NP1. From a structural point of view, it was obvious that the presence of smaller ligaments also meant a larger ligament density and therefore a greater possibility for ligament rearrangement and densification.

For the indent-size effect on hardness, a greater ability for densification meant that a larger, more pronounced gradient density had developed in the deformation zone. We emphasize here that use of a bad practice during nanoindentation can lead to an incorrect evaluation of the materials' properties. Of course, first, the depth dependence may lead to overestimation of the materials' hardness (this is true for all materials). Second, and probably much more detrimental, is misleading comparisons. In our research, NP1 softer than NP2 shows a larger slope in the plot of H as a function of $1/h$ (Figure 6c,d). This leads to an inversion in apparent hardness; NP1 has a higher hardness when compared to NP2 below an average critical depth of around 150 nm. A similar trend was observed for metallic glasses [24].

5. Conclusions

The depth dependence of an NP's hardness, as measured using nanoindention in DMA mode, was studied for nanoporous silver prepared by dealloying an $Ag_{38.75}Cu_{38.75}Si_{22.5}$ precursor. Two near-similar NPs were analyzed and compared. These materials were composed of connected ligaments with various levels of surface shape and curvedness, which was revealed in our experiment by tomographic imaging. For the two NPs, the hardness-dependence indent depth followed a rule of the form $H/H_0 = 1 + h^*/h$, first identified empirically and then compared to a description based on the strain-gradient approach proposed by Ashby and the densification rule for granular materials proposed by Shapiro–Kolthoff.

From these analyses, two main conclusions must be emphasized. First, heterogeneity of NPs at the length scale of the indent probe produced significant scattering in the results but systematic linear dependence of H as a function of $1/h$. This enabled us to evaluate the relevant hardness with far less scattering and by extrapolating at an infinite indent size $(1/h \to 0)$. Second, the proposed analytical description confirmed that the porosity level (as in the Gibson–Ashby scaling law) was not the only essential parameter controlling densification during the NPs' plastic deformation process.

The length scale was derived from the Ashby strain-gradient approach and the kinetic constant from the 1st order law of Shapiro–Kolthoff, which became dominant at the nanometer scale. These two parameters were both related to the local structure of ligaments and their ease of rearrangement, which also included their size and overall topological features. Nanoindentation was proven to be a useful technique for investigating the structural properties of NPs but further analysis should be performed in connection with 3D tomography characterization so as to relate NP structural characteristics with their mechanical behavior.

Author Contributions: D.B. prepared nanoporous metals and participated to all characterization and data analyses; A.M.J.J. and Y.C. supervised the work and results interpretation; F.C. carried out F.I.B. experiments. M.L.-B. carried out nano-indentation experiments; P.L. performed and analysed 3D imaging. Y.C. developped the model; All authors participated in writing and reading the paper.

Funding: This work was supported by the European ITN Network project "VitriMetTech" (grant No. FP7-PEOPLE-2013-ITN-607080) in the framework of the Marie Sklodowska-Curie actions program. The program and works on nanoporous metals were initiated by Alain Reza Yavary (SIMaP CNRS G-INP). YC, AMJJ, and DB dedicate this article to his memory.

Conflicts of Interest: The authors declare no conflict of interest.

References

1. Weissmuller, J.; Newman, R.C.; Jin, H.J.; Hodge, A.M.; Kysar, J.W. Nanoporous Metals by Alloy Corrosion: Formation and Mechanical Properties. *MRS Bull.* **2009**, *34*, 577–586. [CrossRef]
2. Mameka, N.; Wang, K.; Markmann, J.; Lilleodden, E.T.; Weissmuller, J. Nanoporous Gold-Testing Macro-scale Samples to Probe Small-scale Mechanical Behavior. *Mater. Res. Lett.* **2016**, *4*, 27–36. [CrossRef]
3. Badwe, N.; Chen, X.Y.; Sieradzki, K. Mechanical properties of nanoporous gold in tension. *Acta Mater.* **2017**, *129*, 251–258. [CrossRef]
4. Jin, H.J.; Weissmuller, J. A Material with Electrically Tunable Strength and Flow Stress. *Science* **2011**, *332*, 1179–1182. [CrossRef] [PubMed]
5. Jin, H.J.; Weissmuller, J.; Farkas, D. Mechanical response of nanoporous metals: A story of size, surface stress, and severed struts. *MRS Bull.* **2018**, *43*, 35–42. [CrossRef]
6. Fujita, T.; Tokunaga, T.; Zhang, L.; Li, D.W.; Chen, L.Y.; Arai, S.; Yamamoto, Y.; Hirata, A.; Tanaka, N.; Ding, Y.; et al. Atomic Observation of Catalysis-Induced Nanopore Coarsening of Nanoporous Gold. *Nano Lett.* **2014**, *14*, 1172–1177. [CrossRef]
7. Chen, Q.; Ding, Y.; Chen, M.W. Nanoporous metal by dealloying for electrochemical energy conversion and storage. *MRS Bull.* **2018**, *43*, 43–48. [CrossRef]
8. Seker, E.; Berdichevsky, Y.; Staley, K.J.; Yarmush, M.L. Microfabrication-Compatible Nanoporous Gold Foams as Biomaterials for Drug Delivery. *Adv. Healthc. Mater.* **2012**, *1*, 172–176. [CrossRef]
9. El-Safty, S.A.; Hoa, N.D.; Shenashen, M.A. Topical Developments of Nanoporous Membrane Filters for Ultrafine Noble Metal Nanoparticles. *Eur. J. Inorg. Chem.* **2012**, *2012*, 5439–5450. [CrossRef]
10. Juarez, T.; Biener, J.; Weissmuller, J.; Hodge, A.M. Nanoporous Metals with Structural Hierarchy: A Review. *Adv. Eng. Mater.* **2017**, *19*, 1700389. [CrossRef]
11. Seker, E.; Reed, M.L.; Begley, M.R. Nanoporous Gold: Fabrication, Characterization, and Applications. *Materials* **2009**, *2*, 2188–2215. [CrossRef]

12. Vargas-Martinez, J.; Estela-Garcia, J.E.; Suarez, O.M.; Vega, C.A. Fabrication of a Porous Metal via Selective Phase Dissolution in Al-Cu Alloys. *Metals* **2018**, *8*, 378. [CrossRef]
13. Ziehmer, M.; Hu, K.X.; Wang, K.; Lilleodden, E.T. A principle curvatures analysis of the isothermal evolution of nanoporous gold: Quantifying the characteristic length-scales. *Acta Mater.* **2016**, *120*, 24–31. [CrossRef]
14. Jiao, J.; Huber, N. Deformation mechanisms in nanoporous metals: Effect of ligament shape and disorder. *Comput. Mater. Sci.* **2017**, *127*, 194–203. [CrossRef]
15. Storm, J.; Abendroth, M.; Emmel, M.; Liedke, T.; Ballaschk, U.; Voigt, C.; Sieber, T.; Kuna, M. Geometrical modelling of foam structures using implicit functions. *Int. J. Solids Struct.* **2013**, *50*, 548–555. [CrossRef]
16. Lilleodden, E.T.; Voorhees, P.W. On the topological, morphological, and microstructural characterization of nanoporous metals. *MRS Bull.* **2018**, *43*, 20–26. [CrossRef]
17. Barsuk, D.; Zadick, A.; Chatenet, M.; Georgarakis, K.; Panagiotopoulos, N.T.; Champion, Y.; Jorge, A.M. Nanoporous silver for electrocatalysis application in alkaline fuel cells. *Mater. Des.* **2016**, *111*, 528–536. [CrossRef]
18. Lawn, B.; Wilshaw, R. Indentation fracture principles and applications. *J. Mater. Sci.* **1975**, *10*, 1049–1081. [CrossRef]
19. Hutchings, I.M. The contributions of David Tabor to the science of indentation hardness. *J. Mater. Res.* **2009**, *24*, 581–589. [CrossRef]
20. Yuan, Z.W.; Li, F.G.; Chen, B.; Xue, F.M. The correlation between indentation hardness and material properties with considering size effect. *J. Mater. Res.* **2014**, *29*, 1317–1325. [CrossRef]
21. Ashby, M.F. The deformation of plastically non-homogeneous materials. *Philos. Mag.* **1970**, *21*, 399–424. [CrossRef]
22. Nix, W.D.; Gao, H.J. Indentation size effects in crystalline materials: A law for strain gradient plasticity. *J. Mech. Phys. Solids* **1998**, *46*, 411–425. [CrossRef]
23. Huang, Y.J.; Shen, J.; Sun, Y.; Sun, J.F. Indentation size effect of hardness of metallic glasses. *Mater. Des.* **2010**, *31*, 1563–1566. [CrossRef]
24. Champion, Y.; Perriere, L. Strain Gradient in Micro-Hardness Testing and Structural Relaxation in Metallic Glasses. *Adv. Eng. Mater.* **2015**, *17*, 885–892. [CrossRef]
25. Zhang, M.; Jorge Junior, A.M.; Pang, S.J.; Zhang, T.; Yavari, A.R. Fabrication of nanoporous silver with open pores. *Scr. Mater.* **2015**, *100*, 21–23. [CrossRef]
26. Boulos, V.; Salvo, L.; Fristot, V.; Lhuissier, P.; Houzet, D. Investigating performance variations of an optimized GPU-ported granulometry algorithm. In Proceedings of the 18th International European Conference on Parallel and Distributed Computing, Rhodes Island, Greece, 27–31 August 2012.
27. Oliver, W.C.; Pharr, G.M. An improved technique for determining hardness and elastic-modulus using load and displacement sensing indentation experiments. *J. Mater. Res.* **1992**, *7*, 1564–1583. [CrossRef]
28. Shapiro, I.; Kolthoff, I.M. Studies on the Aging of Precipitates and Coprecipitation. XXXVIII. The Compressibility of Silver Bromide Powders. *J. Phys. Chem.* **1947**, *51*, 483–493.
29. Ashby, M.F.; Evans, A.G.; Fleck, N.A.; Gibson, L.J.; Hutchinson, J.W.; Wadley, H.N.G. *Metal Foams: A Design Guide*; Butterworth Heinemann: Boston, MA, USA, 2000.
30. James, P.J. Particle deformation during cold isostatic pressing of metal powders. *Powder Metall.* **1977**, *20*, 199–204. [CrossRef]